Journal of Alloys and Metallurgical Systems 6 (2024) 100074

Contents lists available at ScienceDirect

Journal of Alloys and Metallurgical Systems

journal homepage: www.journals.elsevier.com/journal-of-alloys-and-metallurgical-systems

Tribo-electrochemical investigation of 60NiTi alloy in saline solution

Anthony Onyebuchi Okoani [a,c,*], Ashveen Nand [b], Maziar Ramezani [a,**]

[a] Department of Mechanical Engineering, Auckland University of Technology, Auckland, New Zealand
[b] Faculty of Engineering, University of Auckland, New Zealand
[c] Department of Mechanical Engineering, University of Nigeria, Nsukka, Nigeria

ARTICLE INFO

Keywords:
3.5 wt% NaCl electrolyte
NiTiNOL60 alloy
Three-body abrasion
Corrosion-wear
Oxidation
Wear mechanisms

ABSTRACT

This research explores the tribocorrosion behaviour of 60NiTi alloy, also known as NiTiNOL60, when exposed to a saline environment. Our investigation focuses on understanding the relationship between corrosion and wear rates and assessing surface damage and material degradation. To conduct our experiments, we employed a linear reciprocating ball-on-plate tribometer coupled with electrochemical polarisation using a three-electrode cell configuration to assess the combined effects of corrosion and sliding wear. Surface characterisation was carried out through scanning electron microscopy and energy dispersion spectroscopy, revealing the material to be a Ni-rich 60NiTi alloy, with surface oxidation evident in the electrolyte medium. Our electrochemical findings indicate the occurrence of localised corrosion in both cathodic and anodic regimes, with corrosion pit nucleation, cavities, and cracks being accelerated by reciprocating sliding and corrosion potential. These interactions exposed the material surface to various wear mechanisms, including abrasive, adhesive, oxidative, corrosive, and fatigue processes. This study underscores the significant influence of mechanical properties on the rate of material degradation due to corrosion, while also highlighting the substantial impact of prevailing electrochemical conditions on the rate of mechanical material removal. This paper offers valuable insights for designers working on load-bearing structures in saline environments.

1. Introduction

In recent years, there has been a growing interest in understanding the performance of Nickel-Titanium (NiTi) alloys in corrosive environments [1,2]. This stems from the recognition that corrosion plays a vital role in tribocorrosion systems, impacting both engineering [3,4] and medical applications [5,6]. The significance of corrosion is particularly pronounced in marine environments, where materials often face surface damage and material loss due to the corrosive nature of the surroundings [7,8]. Several factors influence corrosion in these environments, including the metal's position in the electrochemical series, pH levels, presence of electrolytes, metal impurities, oxygen concentration, and temperature variations [9]. Offshore applications subject materials to extreme environmental conditions, hastening their degradation. In such marine environments, multiple concurrent phenomena, including tribocorrosion, can reduce the lifespan of structural materials and lead to unexpected failures.

Traditional materials like high-strength steels are commonly used in offshore structural applications due to their favourable strength-to-weight ratios [7]. However, their low alloy content in elements that promote passive film formation, such as Chromium (Cr), Nickel (Ni), and Molybdenum (Mo), results in the formation of a porous and weakly adherent ferric oxyhydroxide (FeOOH) compound on the surface [10]. This porous rust film allows the electrolyte to penetrate and reach the bare steel, perpetuating corrosion and material loss. Consequently, low-alloyed steels are susceptible to corrosion even in their intended applications. For example, tribocorrosion plays a crucial factor in the premature failure of components within mooring systems [7], underscoring the complex interaction between wear and corrosion. While passive materials like stainless steels and titanium alloys are known for their resistance to tribocorrosion in various corrosive environments, their high cost limits their use in offshore applications compared to lower-alloyed steels that satisfy mechanical requirements at the expense of corrosion resistance. Alternative materials, such as conventional steel-based bearing materials (e.g., M50 and 52100), while electrically conductive and magnetically suitable, are prone to corrosion if not adequately protected [11,12].

High-performance bearings, gears, and mechanical components

* Corresponding author at: Department of Mechanical Engineering, Auckland University of Technology, Auckland, New Zealand.
** Corresponding author.
E-mail addresses: anthony.okoani@aut.ac.nz (A.O. Okoani), maziar.ramezani@aut.ac.nz (M. Ramezani).

https://doi.org/10.1016/j.jalmes.2024.100074
Received 24 October 2023; Received in revised form 3 April 2024; Accepted 21 April 2024
Available online 22 April 2024

require specific attributes, including high strength, hardness, thermal conductivity, precision manufacturing, and surface finish capabilities [11]. According to Meddah, et al. [13], Titanium alloys have gained traction for aerospace and other applications such as the biomedical, automotive and energy industries. In spacecraft systems, bearings are expected to tolerate transient loads from launch-related vibration and environmental corrosion, such as from corrosive ambient marine conditions [14]. However, this alloy's low transformation temperature and poor dimensional stability must be addressed to employ it as structural and load-bearing components in aircraft applications.

Metallic alloys with a significant Titanium (Ti) content tend to be suboptimal tribological materials, struggling to respond effectively to lubrication and unable to withstand loads, making them unsuitable for moving mechanisms and tribological applications [11,15,16]. Highly alloyed stainless steel, such as superduplex grades, offers mechanical properties and high corrosion resistance but remains susceptible to localised corrosion types like pitting and crevice corrosion despite overall corrosion resistance [17]. In addition, the high density of materials leads to high centrifugal forces and limited fatigue life when used as bearing rolling elements. These factors have prompted the need for a more suitable material or metallic alloy that meets the aerospace requirements for excellent corrosion resistance and good tribological properties, especially for applications in extreme environments.

As a result, NiTi-based alloys have emerged as promising alternatives for bearings and potential offshore structural materials, boasting a unique combination of characteristics, including low density, high specific strength, low Young's modulus, superelasticity, biocompatibility, shape memory effects, and excellent corrosion resistance [15]. Table 1 compares the thermophysical and mechanical properties of NiTiNOL60 alloy and the conventional engineering materials in which NiTiNOL60 alloy tends to replace in load-bearing and corrosive applications [14,16]. The Table shows that NiTiNOL60 has a low Young's modulus compared to steel while maintaining a similar hardness.

Ni-rich NiTi alloys have gained increasing interest for specialised bearing and gear applications, especially in corrosive environments [18]. For instance, NiTiNOL60 alloy was developed to replace bearings experiencing corrosion and wear issues in the water recovery system of the International Space Station due to its superior mechanical and functional properties [18]. Research has shown that load bearing, tribological, and time-temperature-transition behaviours of Ni-rich compounds play critical roles in such systems [18,19]. The Ni content in Ni-Ti-based alloys significantly influences phase transformation temperatures. It alters the specific temperatures where austenitic NiTi transforms to martensitic NiTi, affecting the key mechanical and thermal properties [20].

60NiTi, also referred to as NiTiNOL60, is an equi-atomic, ordered intermetallic alloy composed of 60 wt% Ni and 40 wt% Ti. Its distinctive combination of high hardness, low apparent elastic modulus, light weight and resistance to aqueous corrosion make it an attractive candidate for aerospace and marine/offshore applications, particularly as a bearing material and in lubricated spacecraft triboelements [11,14,21]. The unique properties and shape-memory effect of Ni-Ti-based alloys have generated substantial scientific interest [16]. Accordingly, Meddah et al. [13] investigated the sliding wear performance of NiTi alloy annealed with different nickel contents. They found that the higher the Ni concentration, the more resistant the material was to adhesive and abrasive wear, which in turn decreased the wear rates that typically rose with applied load. Another study examined the microstructural evolution, mechanical properties, and oxidation performance of highly Ni-rich NiTi alloys with added V through vacuum arc melting. Their study revealed that while V content above 3 at% changed the morphology and distribution of the Ni_3Ti_2, increased the hardness of the alloy, the V content less than 3 at% improved the oxidation resistance of the binary 60NiTi alloy at 500 ℃ [22]. Given the considerable attention surrounding NiTi alloys, previous research can be categorised into several areas: basic corrosion and electrochemical studies, mechanical and material property investigations, and surface treatment studies [2]. However, the need for tribocorrosion investigations became apparent as tribological and electrochemical factors interact in complex ways [23]. Previous studies have shown that the electrochemical material removal rate depends on mechanical parameters while prevailing electrochemical conditions influence the mechanical material removal rate. The synergistic interaction of wear and corrosion leads to more significant material loss compared to their individual effects [24]. As reported by Muñoz and Espallargas [25], the mechanism of fretting corrosion involves both mechanical and chemical components, with the observable damage typically coming from both. Further, Yan, et al. [26] highlighted that the mechanistic method separates the two primary contributions into mechanical wear and anodic dissolution (wear-accelerated corrosion).

Following the high level of surface damage and material loss due to tribocorrosion in corrosive environment often represented by a 3.5 wt% NaCl (artificial seawater) solution which depicts the environment where some engineering materials, including NiTi alloy, Ti-based alloys, stainless steels etc., commonly face deterioration, especially in load bearing applications. Various studies have investigated the tribocorrosion of these materials in artificial seawater environment, but there is still a limited information on the tribocorrosion of NiTi in seawater environment. Ti-6Al-4 V and Monel K500 alloys siding against 316 stainless steel were investigated by Chen and Yan [27]. According to their results, the samples experienced larger wear losses in seawater compared with distilled water [27]. Ayyagari, et al. [28] studied high entropy alloys in dry and marine environments. According to their findings, at accelerated electrochemical corrosion, the sample ($Al_{0.1}$CoCrFeNi) displayed a higher degree of passivation, a higher pitting resistance, and a lower rate of corrosion. In their study, Yan, et al. [26] employed a unidirectional tribological technique to study the microstructure, phase and tribocorrosion behaviour of 60NiTi alloy. Their findings showed that corrosion and tribocorrosion resistance of 60NiTi alloy were improved by solution treatment. Alkan and Gök, [29] examined the effect of sliding wear on AISI 316 stainless steel in seawater. Their results revealed the role of electrochemical potential (i.e., cathodic potential shift towards the anodic potential) in material loss. Based on the wear impact, Gao et al. [30] investigated the behaviour of YSZ coating deposited on stainless steel substrate in a saline solution. Their study revealed that despite the protective layer, an increase in potential significantly increased the material loss of 304 stainless steel as well as the YSZ coating [30]. Consequently, this study aims to address the existing research gap by employing a bidirectional tribocorrosion technique to investigate the synergistic behaviour of NiTiNOL60 alloy in a saline electrolyte, mimicking conditions relevant to offshore and spacecraft applications.

Table 1
Comparing the properties of NiTiNOL60 with other conventional bearing alloys.

Property	NiTiNOL60	440 C	M-50
Density (g/cc)	6.7	7.7	8.0
Hardness (HRC)	52 – 62	58 – 62	60 – 65
Thermal conductivity (W/m-°K)	~9–14	24	~36
Tensile/ (Flexural strength) (MPa)	~1000 (1500)	1900	2500
Young's Modulus (GPa)	~95	200	210
Poisson's ratio	~0.34	0.3	0.3
Fracture toughness (MPa/$\sqrt{m}$)	~20	22	20 – 23
Electrical resistivity (Ω-m)	$\sim 1.04\times10^{-6}$	$\sim 0.60\times10^{-6}$	$\sim 0.18\times10^{-6}$
Max. Temp. use (℃)	~400	~400	~400
Magnetic	Non	Magnetic	Magnetic
Corrosion resistance	Excellent (Aqueous and acidic)	Marginal	Poor

2. Materials and experimental methods

The NiTiNOL60 (60 wt% Ni and 40 wt% Ti) plates were received from the National Aeronautics and Space Administration (NASA), Glenn Research Centre in Cleveland, Ohio. The samples were produced using the Hot Isostatic Pressing (HIP) technique, and Stanford [31] reported detailed information about the fabrication process of the NiTiNOL60 components. To investigate the actual material on an oxide-free surface, the samples were abraded using a Buehler-EcoMet 30 machine for wet grinding with Silicon Carbide (SiC) #180, 500, 1200, and 2400 grit sandpapers having corresponding grain sizes of 104, 35, 15, and 8 μm, respectively. To achieve a mirror surface finish of $\leq$ 0.02 μm, the samples were mechanically polished on a Struers LaboPol-2 machine using diamond paste (6 μm and 1 μm) on a polishing surface of 6 μm and 1 μm, respectively. The polished samples were ultrasonically cleaned for 3 minutes in distilled water and 99.5% (absolute) ethanol before being dried with compressed air. To examine the microstructure, a cross-section of the sample was obtained through the same cutting, abraded, polished, and etched using Kroll's reagent: 82.7% H_2O, 14.1% HNO_3, and 3.2% HF for 30 seconds. The microstructural examinations were performed on the prepared samples (etched and unetched) using an optical microscopy AMScope Olympus BX51 and Hitachi SU-70 scanning electron microscope (SEM) coupled with energy dispersion spectroscopy (EDS) at varying magnifications to determine the microstructural arrangement, surface morphology as well as the elemental distribution in specific regions. Before subjecting the samples to tribocorrosion testing, the roughness of the polished surface was ascertained using a Talysurf 50 Taylor Hobson stylus profilometer and the micro and macro hardness of the sample were measured using Leco microhardness LM–800AT and a Rockwell hardness tester HR–150 A. For the microhardness tests, the specimen was clamped, focused, and tested with 1.0 kgf within a dwell time of 10 seconds. Then, the hardness was calculated by measuring the geometrical aspect of the indentation, such as the surface area or depth of the diamond shape indented on the examined surface. As for the macro indentation hardness test, a combination of major and minor loads (140 + 10) kg summing up to 150 kg were loaded and unloaded, and the resulting values were recorded.

Further preparation of the polished sample was carried out to ensure the sample surfaces, except the top surface with an exposed area of 2 cm^2 were insulated with non-conductive copper tape and plasti-Dip coating. The coating protects the underlying metal against corrosive environments and ensures non-interference during the electrochemical measurements. To carry out the electrochemical measurements, we considered an electrolyte (saline – 3.5 wt% NaCl) suitable for this investigation based on the material's (NiTiNOL60) applications in offshore marine environments. We obtained the aqueous saline solution by dissolving 3.5 wt% of analytical grade reagent NaCl in an equivalent volume of distilled water. The resulting aqueous solution with a pH of 6.3 was used for tribo-electrochemical measurements.

In tribocorrosion measurements, the choice of electrochemical techniques to be employed depends on the contact surfaces' geometries [32]. Considering the shape and flat surface of the specimen and the counter body, a linear reciprocating ball-on-plate tribometer is chosen over a rotary pin-on-disc. The electrochemical method to be incorporated requires a three-electrode cell configuration for measuring open circuit potential (OCP), potentiodynamic polarisation (PDP), and electrochemical impedance spectroscopy [33,34]. This choice for the experimental setup in our investigation was based on the ASTM standard test methods for linear reciprocating ball-on-flat sliding and the synergy between wear and corrosion [35–37]. Thus, the tribocorrosion tests were carried out on a typical linear reciprocating ball-on-plate tribometer (DUCOM TR-282) coupled to an electrochemical workstation (IviumStat potentiostat) of a three-electrode configuration [38].

The test conditions for the reciprocating sliding conditions involve a sliding frequency of 4 Hz, applied normal loads of 2, 5 and 8 N, a stroke length of 10 mm and a total sliding distance of 500 m (resulting in a sliding duration of 6250 seconds) for tribocorrosion test carried out at a room temperature of approximately ~22 ℃. Whereas the conditions for the electrochemical measurements include 1200 seconds for stabilisation at the open circuit potential (OCP), a scan rate of 2 mV/s, applied voltage between −5.0 V to +7.0 V for potentiodynamic measurements within 100 mV potential step for about 60 minutes and a re-conditioning time of 20 minutes. The setup presented in Fig. 1 comprised of the clamped NiTiNOL60 specimen onto a test cell holder serving as the working electrode (WE) and fully immersed in the electrolyte medium, the graphite rod acting as the counter electrode (CE) as well as the calomel reference electrode (RE) filled with 3 M KCl. The counter body was an alumina ball (Al_2O_3) with a Ø 10 mm and surface roughness, R_a of about 0.049 μm ±SD 0.01.

Prior to the tribocorosion test, the system was allowed to attain a steady state during the OCP; afterwards, the simultaneous potentiodynamic polarisation measurements and the reciprocating sliding actions on the contact surfaces (i.e., Al_2O_3 ball sliding against the exposed surface of the NiTiNOL60 sample). During the experiments, the test parameters for electrochemical measurements and coefficient of friction (CoF) were registered on the data acquisition PCs through IviumSoft and WINDUCOM software tools. To ensure consistency and repeatability, each test was carried out three times, with a fresh surface of Al_2O_3 revealed each time to slide against the stationary NiTiNOL60 sample in the corrosive medium. At the end of each test, the sample was cleaned ultrasonically using absolute ethanol and dried for surface characterisations of the wear tracks using SEM / EDS examinations to reveal the wear mechanisms, as well as hardness and roughness measurements.

Following the wear scar on the surface, it is evident that tribocorrosion is a surface alteration that involves the joint actions of relatively moving mechanical contact with electrochemical reactions [39]. Hence, there is a need to quantify the material losses during the simultaneous actions. This involves using a stylus profilometer (Talysurf 50, Taylor Hobson) to measure the surface roughness of the wear tracks and the wear volumes at different applied loads. Five different areas of the wear tracks were examined for the wear volume measurements. This follows the stylus tip moving vertically along the wear track, showing an established two-dimensional output of a surface height and distance along the measured line. The output information was obtained as a raw profile chart showing the sample's worn surface roughness, waviness, asperities, grooves, etc. The profiles in graphical representation enabled the measurements of the dimensions (depth and width) of the wear scars. As a result, we employed ImageJ, a software tool for image analysis, to determine the dimensions of the wear scars. The estimated parameters were then used to calculate the area of the wear track, while the volume loss was obtained by multiplying the area with the reciprocating stroke length (i.e., the wear track length) of 10 mm. With the wear volume acquired, we used Eq. (1), obtained from Archard's wear law expression, to compute the specific wear rate. The wear rate quantifies the material worn under specific operating conditions per unit time.

$$\text{Specific wear rate, } \dot{W}\left(mm^3/N.m\right) = \frac{V}{w.d} \tag{1}$$

where V is the wear volume (mm^3), w represents the normal load (N), and d is the sliding distance (m). For the electrochemical parameters, we extracted the data from the IviumSoft tool; however, the values can also be calculated using the following Butler-Volmer expression presented in Eq. (2). The equation shows a combined Tafel equation for the cathodic and anodic regions in an electrochemical system.

$$I = I_{corr}\left(e^{\frac{2.303(E-E_{corr})}{\beta_a}} - e^{\frac{-2.303(E-E_{corr})}{\beta_c}}\right) \tag{2}$$

where I = current, I_{corr} is the corrosion current, E is the applied potential, E_{corr} is the corrosion potential, and β_a and β_c are the Tafel constants or Tafel slopes derived from the tangential plots at the anodic and

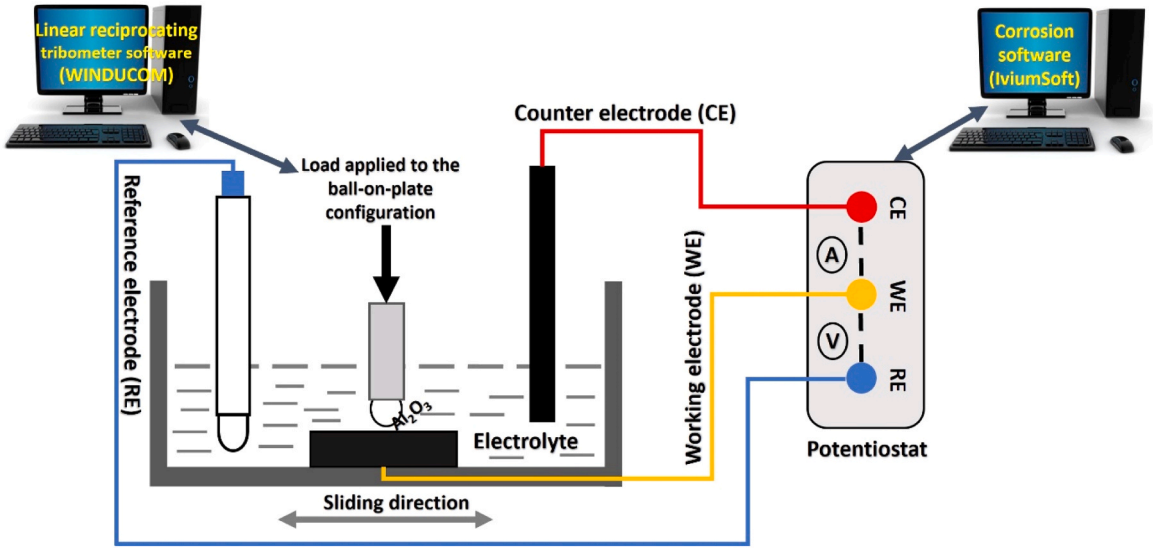

Fig. 1. Experimental setup of a linear reciprocating ball-on-plate tribocorrosion.

cathodic regions, respectively. With the estimated corrosion current from Eq. (2), the expression presented by Rodríguez-Bravo, et al. [40] in Eq. (3) will be used to calculate the corrosion rate considering the exposed area of the sample.

$$\text{Corrosin rate, C.R(mmpy)} = \frac{0.13A * i_{corr} * M}{n * \rho} \tag{3}$$

where I_{corr} = corrosion current density (A/cm^2), A = area (cm^2), M = atomic mass of the metal (g/mol), n = number of electrons/atoms produced or consumed in the redox reaction while ρ = density of the material (g/cm^3), and 0.13 = time conversion factor per unit area of the exposed surface. To quantify the overall wear based on the synergy, Muñoz and Espallargas [25] present the mechanistic interpretation of the tribocorrosion phenomenon [41], i.e., the total wear volume (V_t) as the sum of the material loss due to sliding wear (V_{mech}) and the loss of material due to corrosion or electrochemical oxidation (V_{chem}) expressed in Eq. (4)[26].

$$V_t = V_{mech} + V_{Chem} \tag{4}$$

3. Results and discussions

3.1. Sample characterisations and metallographic investigations

The SEM and EDS surface characterisation techniques examined the oxide-free (mirror finish) surface samples. Fig. 2 displays the NiTiNOL60 SEM micrograph and the EDS quantitative composition analysis. The sample surface was scanned at full scale using a penetrating voltage of 20 KV. By using a high penetrating voltage, it is possible to generate X-rays from deeper inside the sample subsurface, allowing for a thorough investigation of both the sample's surface and subsurface regions. EDS (point-and-shot and spectral imaging) technique was employed to quantify the elemental compositions along the wear track of the specimen. While the point-and-shoot method examined specific points as Fig. 5 shows, the spectral imaging measured the entire surface for an overall quantification as shown in Fig. 6., with the respective elemental composition in weight percentage of the elements. The characterisation results (SEM and EDS) of the polished sample presented in Fig. 2 confirmed only the presence of the non-equiatomic sample composed of Ni and Ti elements of 59.26 and 40.74 wt%, respectively with no trace of any other element, thereby confirming the sample as a Ni-rich 60NiTi alloy. Further, the determination of the surface oxidation on the wear

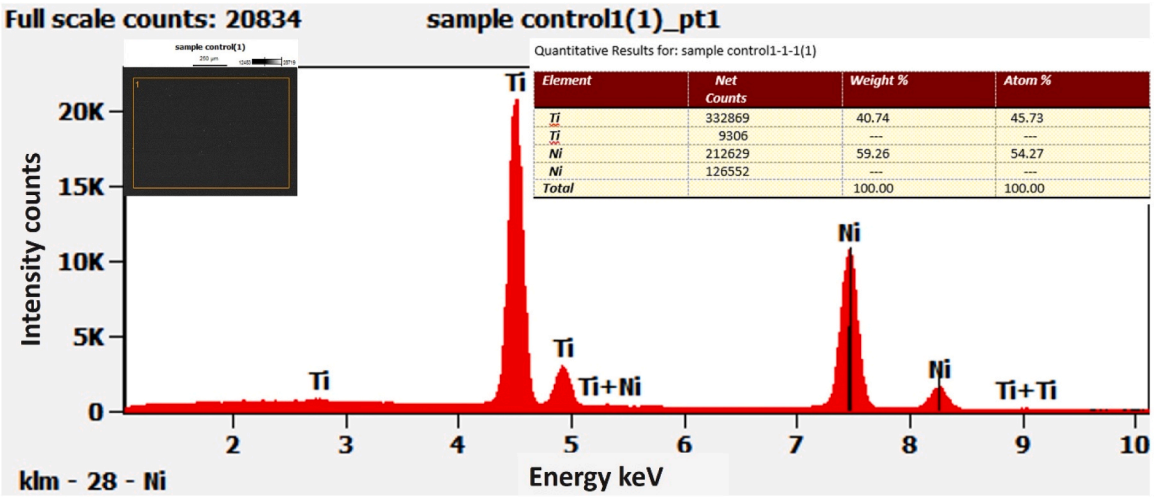

Fig. 2. SEM and EDS surface characterisation of NiTiNOL60 alloy.

track surface was determined using spectral imaging and point-and-shot methods to ascertain the elemental composition and distribution along the wear track. Fig. 6 shows the elemental distribution within certain regions along the wear track. The micrographs clearly show the concentration of each element. Hence, the EDS results confirm that the sample under investigation is a Ni-rich 60NiTi alloy possessing approximately the same weight percentage compositions of 60 and 40 for Ni and Ti, respectively, which aligns with the literature information reported by previous researchers [42,43].

Further examination of the surface on a microscopic scale reveals the microstructural composition of the sample. This was achieved through a cross-sectional part of the sample obtained using wire cutting, and the surface was ground, polished and equally etched for the subsurface examination. The micrograph shown in Fig. 3 presents the microstructural arrangements of NiTiNOL60 before tribocorrosion investigation. According to the micrograph, NiTiNOL60 is an ordered intermetallic material compound with cubic and rhombohedral crystal matrix structures, supporting earlier researchers' observations [43]. The closely packed grain network of unconsolidated and consolidated grain clusters could be referred to as the existence of inhomogeneity in the microstructural grains [20]. This may be explained by the non-equiatomic composition of NiTiNOL60, which has a propensity for Ni-rich or Ti-rich zones. This affirms the dominance of Ni_4Ti_3 and B2 NiTi matrix as presented in our previous report [24], while Khanlari, et al. [43,44] referred to the phases as cubic and rhombohedral crystal structures. According to Du, et al. [45], the microstructure 60Ni-40Ti is alternately composed of fine and coarse network structures, which are relatively uneven on the microscopic scale, so its microhardness fluctuates more violently.

After the tribo-electrochemical tests in the corrosive environment, the reciprocating sliding between the contact surfaces created a wear track on the examined surface of NiTiNOl60. As a result, we examined the wear tracks using SEM and EDS characterisation at the same penetrating voltage of 20 KV used to examine the untested oxide-free sample to ensure adequate penetration of the rays into the subsurface layers. The surface morphologies of the corroded wear tracks are shown in Fig. 4. The micrographs highlight mild to severe surface degradation caused by mechanical and chemical attacks in the electrolyte medium. The level of corrosion attack shown in Fig. 4 depends on the impact of the applied load. Clearly, corrosion pits and crevices advanced from the nucleation stage to metastable pit formation and then to stable pitting, where the material deforms plastically. This aligns with the existing literature stating that pitting is self-initiating and self-propagating, thereby making it difficult to determine the borders for every stage, such as nucleation, metastable pit formation and stable pitting [46]. From our analysis, the contact pressure on the interacting surfaces promoted corrosion pit nucleation and propagation. The average corrosion pits measured on the corroded surface of 60NiTi wear track generally ranged between 25 and 120 μm.

Following the high level of wear debris attachment, we further analysed the wear track surfaces using EDS to ascertain the composition of the attached wear particles on the surfaces. Fig. 5 presents the EDS surface examination along the wear track using the point-and-shoot approach for a sample surface subjected to a 5 N load. The quantitative elemental composition of examined points confirms the surface oxidation, which promoted the corrosive mechanism shown in Fig. 4. The micrographs also show the adhesion of the wear debris caused by detachment and delamination.

Similarly, the high level of adhesion and distinctive attachment of wear particles observed at the sample surface at an applied load of 8 N prompted further examination. Accordingly, we employed the spectral imaging technique for detailed and distinctive examination. Fig. 6 shows the spectral imaging of the elemental distribution which clearly highlights the concentration of the oxidised areas. As depicted in the micrographs, the regions with higher concentration can easily be identified with the bright areas. The purple micrograph represents the oxidation distribution within the region, while the yellow colour distribution highlights the areas with high adhesion of the counter material debris and the elemental distribution of the contacting surfaces. The blue and red colours show the elemental distributions of the base material spread across the micrographs.

3.2. *Analysis of the reciprocating sliding friction and wear behaviours*

The variations of the coefficient of friction (CoF) during the tests

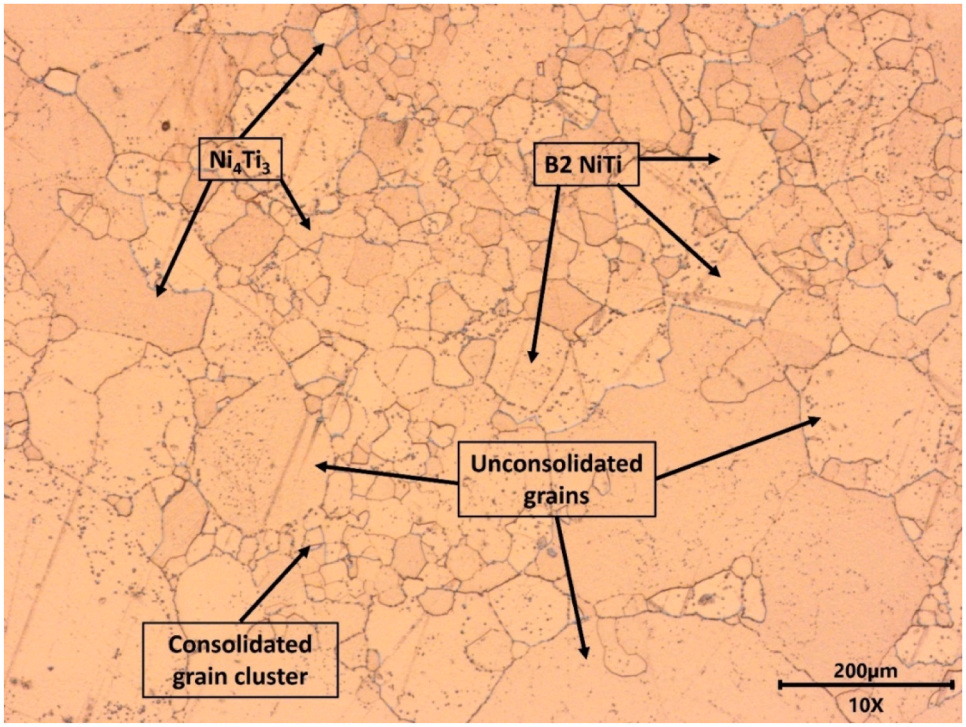

Fig. 3. Optical micrograph of NiTiNOL60 microstructural grain arrangement.

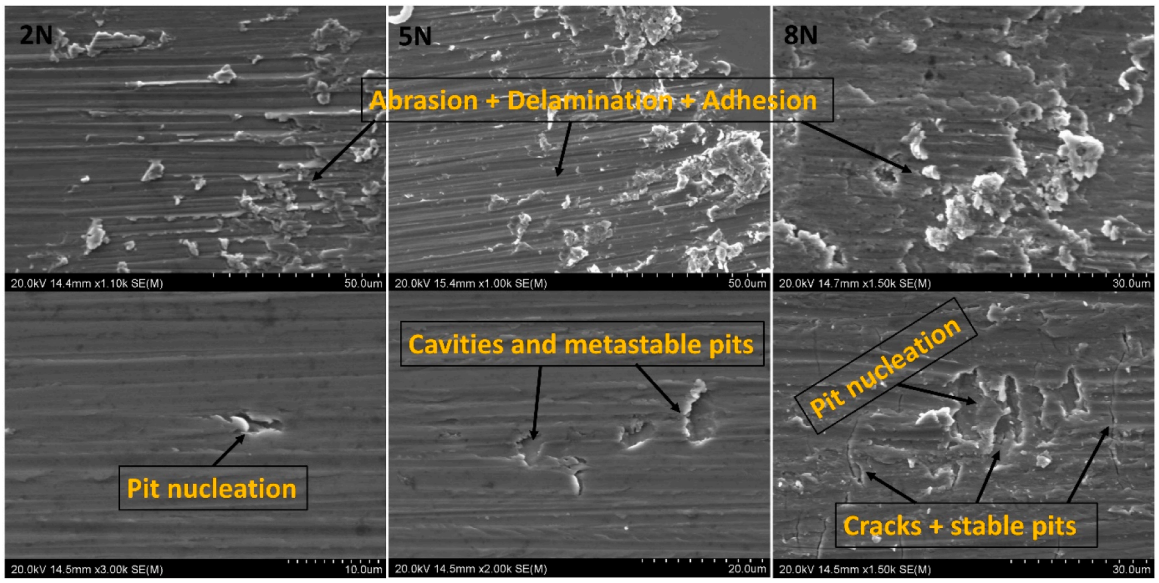

Fig. 4. SEM images showing the wear mechanisms along the wear track under different applied loads.

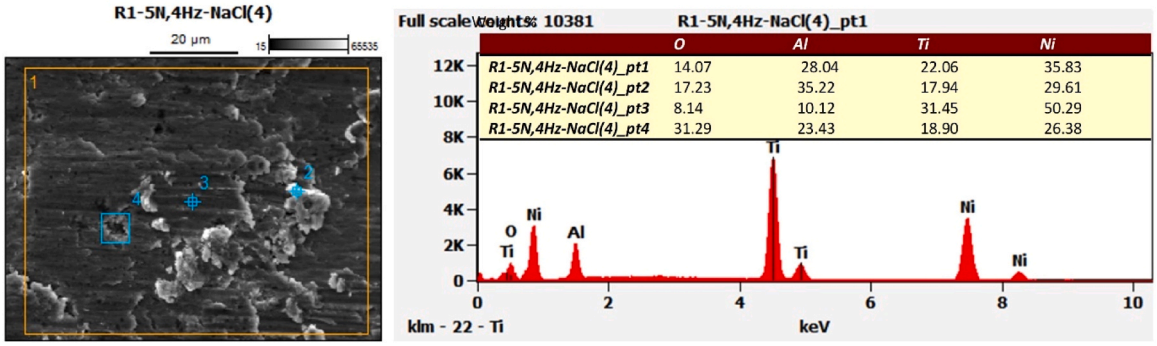

Fig. 5. EDS examination of wear track at an applied load of 5 N.

were analysed to measure the wear behaviour of the material throughout the sliding duration. Fig. 7 presents a similar frictional behaviour for the investigated three applied loads, except for the running-in time recorded at the 2 N load. The initial stage of sliding was characterised by the interfacial friction interactions leading to the breakdown of oxide layers [47,48], localised heating of the contact surfaces and oxidation of asperities. The continuous reciprocating sliding at higher contact pressure wears the passive layers as well as the subsurface of the material [49]. This indicates that any increase in the contact pressure increases the surface roughness and widens the wear track, which creates a larger surface area for oxidation. This is supported by the SEM micrographs in Fig. 4, where the sample surface investigated at 2 N showed the least chemical and mechanical wear mechanisms. It is evident that the highest average coefficient of friction ($\mu = 0.93$) was recorded for the 8 N wear track. This confirms the increased roughness/ wider wear track, the highest wear volume and various wear mechanisms that could possibly result in plastic deformation [50]. The mechanisms were promoted by the high level of detachment as the CoF levels also indicate that friction is most severe at higher loads [51], i.e., 8 N and 5 N (applicable to our study), unlike in the 2 N load where the applied load at 4 Hz showed a gradual material loss (wear) at the interacting surfaces.

Considering the high level of material detachment and adhesion noted in Figs. 5 and 6 and supported by the high average CoF values in Fig. 7, we examined the surface of the counter body (Al_2O_3 ball) sliding against NiTiNOL60 alloy during the tribocorrosion tests using SEM and EDS techniques. Fig. 8 presents the level of adhesion caused by the micro-joint formation [52] between the contact surfaces of the alumina ball and 60NiTi during sliding actions. For the examined surfaces at the three applied loads, an area scan reveals the elemental compositions deposited on the surfaces. The surfaces were oxidised in all the electrolyte mediums, with the oxide concentration decreasing with increased applied load. The highest oxygen concentration was recorded at the 2 N load, while the 8 N load showed the lowest oxygen concentration. This implies that the less contact pressure at the applied load of 2 N was not adequate to breakdown/ wear the oxide layer formed during tribocorrosion, which is supported by the delayed running-in time shown in the CoF plot in Fig. 7. Hence, the validation that the significant impact from the contact pressures at higher applied loads causes detachment of the interacting surfaces, which subsequently results in abrasion and adhesion mechanisms [49]. The adhered wear particles (debris) could be seen for the surfaces at 5 N and 8 N loads, with less pronounced deposits for the ball surface at the applied load of 2 N. Thus, only one point (area scan) was examined for the surface at 2 N, unlike the three to four points examined for the surfaces sliding at the applied loads of 5 N and 8 N following the pronounced adhesion of wear particles. While point 2 in the quantitative result confirms the actual composition of the attached materials to be NiTiNOL60 base materials - Ni and Ti, points 3 and 4 for 8 N and 5 N loads reveal the greater concentration of the alumina ball with little deposits of the specimen.

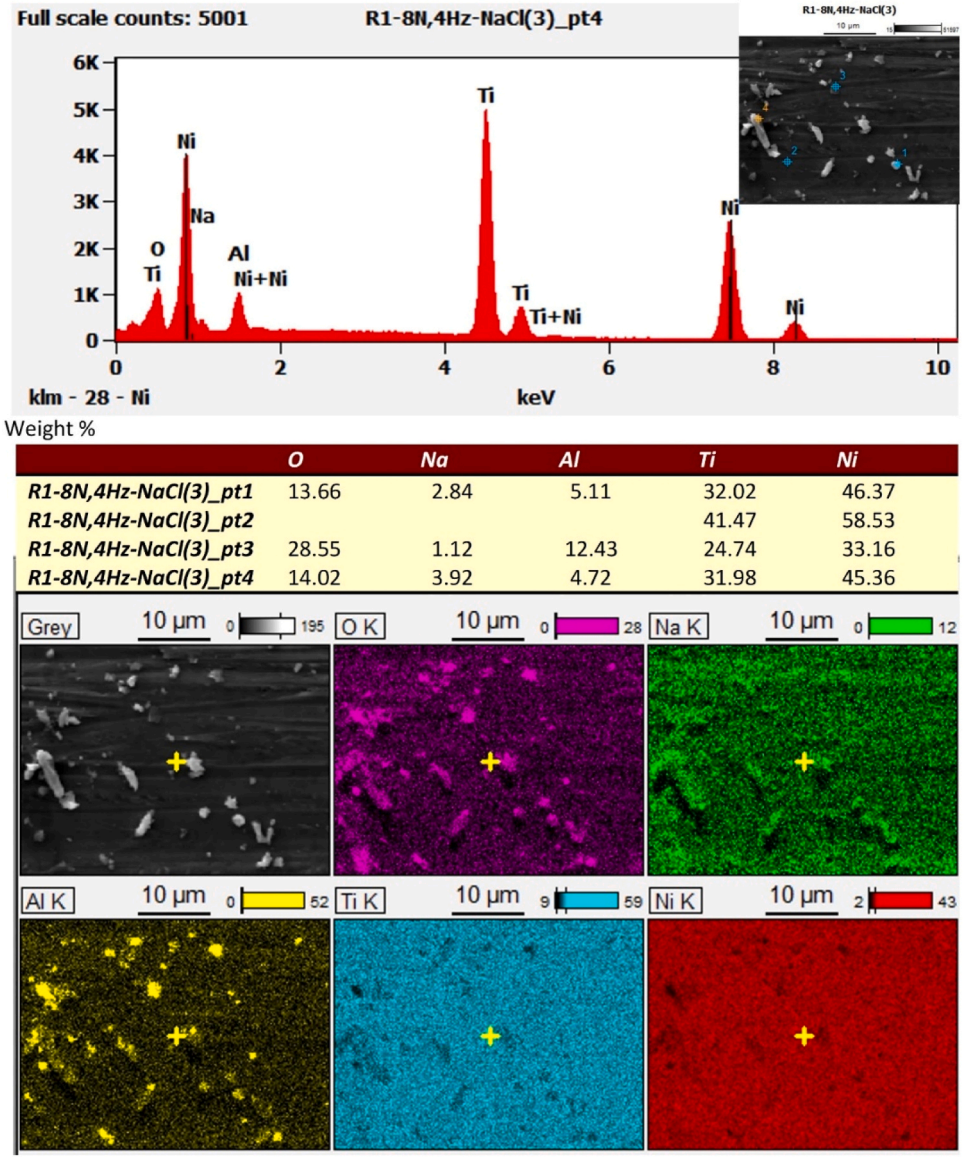

Weight %

	O	Na	Al	Ti	Ni
R1-8N,4Hz-NaCl(3)_pt1	13.66	2.84	5.11	32.02	46.37
R1-8N,4Hz-NaCl(3)_pt2				41.47	58.53
R1-8N,4Hz-NaCl(3)_pt3	28.55	1.12	12.43	24.74	33.16
R1-8N,4Hz-NaCl(3)_pt4	14.02	3.92	4.72	31.98	45.36

Fig. 6. EDS spectral imaging of adhered wear debris on the wear track NiTiNOL60.

3.3. Electrochemical measurements of potentiodynamic polarisation

In electrochemical reactions involving metals and electrolytes, oxidation is prevalent, and this has been confirmed by the SEM and EDS results, as shown in the Figs. 4, 5 and 6. The electrochemical results obtained from this investigation are shown in both tabulated and graphical representations. Table 2 represents the summarised electrochemical parameters obtained through the IviumSoft data acquisition tool during the tribocorrosion measurements. The table denotes that at the open circuit system, which represents the electrochemical activity of the material, parameters such as the corrosion potential, corrosion current density, passivation resistance and corrosion rate estimated were obtained from Tafel analysis. From our study, it could be deduced that an increase in the applied load increased the corrosion current and pushed the corrosion potential towards zero, thereby leading to a continuous drop in the polarisation resistance, which in turn increased the corrosion current. This confirms that a metal's dissolution rate depends on the corrosion potential, which determines the anodic or cathodic polarisation activity [53].

Following the results shown in Table 2, Fig. 9 depicts the potentiodynamic polarisation curves of the sample after immersion in 3.5 wt% NaCl solution and tribocorrosion investigation. The curves depict electrochemical activities that occurred in the cathodic and anodic regimes, resulting in pit nucleation and metastable pit formation, cavities, and cracks [54,55]. Further, it shows a distinct passivation platform area, indicating that a stable passivation film forms on the material's surface within the corresponding self-corrosion voltage range, protecting the base material from corrosion. According to previous reports, the electrochemical breakdown of oxides of some metals is reduced cathodically to the metals or ions in aqueous solutions [46]. In aqueous solutions, solution anions, halides and nonhalide types can play a significant role in passive film growth and breakdown. Halide ions such as Cl^- can give rise to severe localised corrosion (e.g., pitting); this is evident in the SEM micrographs and the Tafel plots showing cavitation that increased significantly as the applied load increased. The surface damages could also be attributed to the continuous destruction of the passivation film which exposed the material subsurface to more corrosion attack and subsequently led to plastic deformation [56]. Evidently, the cavitation shown in Fig. 9 resulting from the adhesion and repassivation on the anode surface, could impede the reactivity between the anode surface and the electrolyte [10,40,57]. As the electrochemical activity proceeds and the passive film dissolves, the system overcomes the driving factors

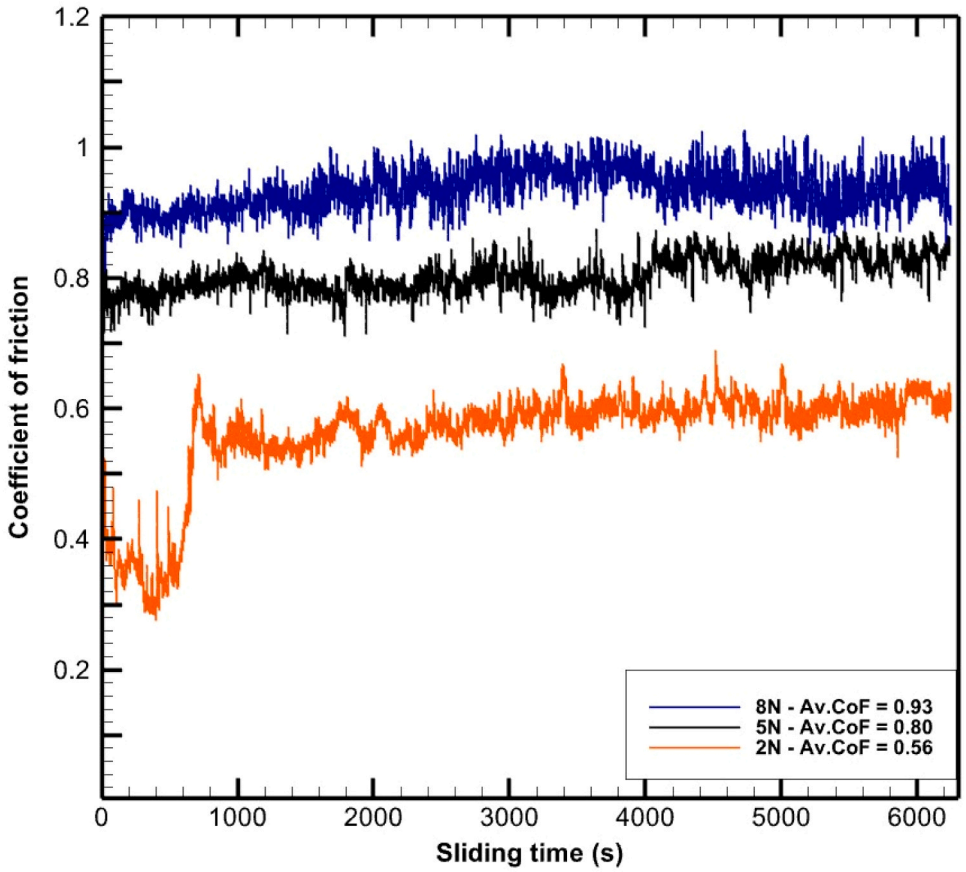

Fig. 7. Plot of friction coefficient against sliding time at different applied loads.

and attains equilibrium as the corrosion potential tends to be more stable [45]. Repassivation generates surface protective oxide film (TiO_2) which offers great resistance in static corrosion, unlike in the combined actions corrosion and mechanical wear [58]. As oxidation progressed, oxygen atoms diffuse towards the NiTi substrate, while Ni atoms diffuse outward on the surface, hence the rich zones of Ni and Ti [56]. The localised corrosion and plastic deformation, which resulted due to the synergistic interactions were promoted by the reactions in both regimes. According to Guadalupe et al. [55], the chemical reaction between metal and water generates a surface metal oxide and releases hydrogen as demonstrated in Eq. 5.

$$Me + H_2O \rightarrow MeO_x + xH_2 \quad (5)$$

Further, Vilhena et al. [54] reported that the electrochemical behaviour (reduction reactions) that take place at the cathodic branch are dependent on the nature of the corrosive environment, for instance the oxygen reduction in alkaline medium as represented in Eq. 6.

$$O_2 + 2H_2O + 4e^- \rightarrow 4OH^- \quad (6)$$

3.4. Wear mechanisms

The simultaneous reciprocating sliding and electrochemical potential activities promoted the various wear mechanisms [29,59] recorded in this investigation. Based on the wear synergy, we quantified the results using the methods and equations outlined in Section 2 to depict the wear volume, specific wear rate and corrosion rate, as presented in Fig. 10. The mechanistic approach distinguishes between two critical contributions of mechanical wear and anodic dissolution, i.e., wear-accelerated corrosion [24,60]. From the plots, it is evident that an increase in the applied normal load increased the wear volume, corrosion rate and specific wear rate due to the synergistic interaction. The tribocorrosion interaction promotes the shearing of asperities following sliding and frictional heating at the contact interfaces which consequently results in large surface deformation [61]. During the tests, reciprocating sliding removes the passive film and promotes enhanced anodic metal oxidation on the bare metal until repassivation [56]. This results in a sudden cathodic shift of the potential towards the negative but stabilises with a drop in corrosion current as the system attains steady state. The cathodic shift, however, is less noticeable at lower loads where less surface damage occurs. The formation of cavities is promoted by the presence of voids on the sample's surface, which potentially elongated to the subsurface. The combined effects of void formation as well as the intermetallic phase distortion result in increased surface roughness and a larger friction coefficient [45,62]. These synergistic interactions supported by the third-body abrasion recorded at higher applied loads result in significant surface damage (localised corrosion and plastic deformation). Hence, the material loss occurring due to the synergism between wear and corrosion is more significant when compared to their individual impacts [9,23]. The results clearly show that the localised corrosion of the material was controlled by oxidation of the alloy in the anodic regime, which subsequently resulted in the metallic dissolution. The graphical trends illustrating a continual increase in corrosion and wear rates validate that the halide ions in the electrolyte gave rise to wear-accelerated corrosion.

Fig. 11 illustrates a summarised tribocorrosion wear mechanism of NiTiNOL60 alloy investigated in the saline environment. Our analysis deduced that all the sample surfaces examined under the different loads were oxidised. While the oxidised surfaces promoted localised corrosion as confirmed with the SEM and EDS examinations, the sliding contacts initiated the breakdown of oxide/ passive films [26], which led to delamination, followed by mild to severe abrasion, adhesion and subsequently to plastic deformation of the material. The contact pressure

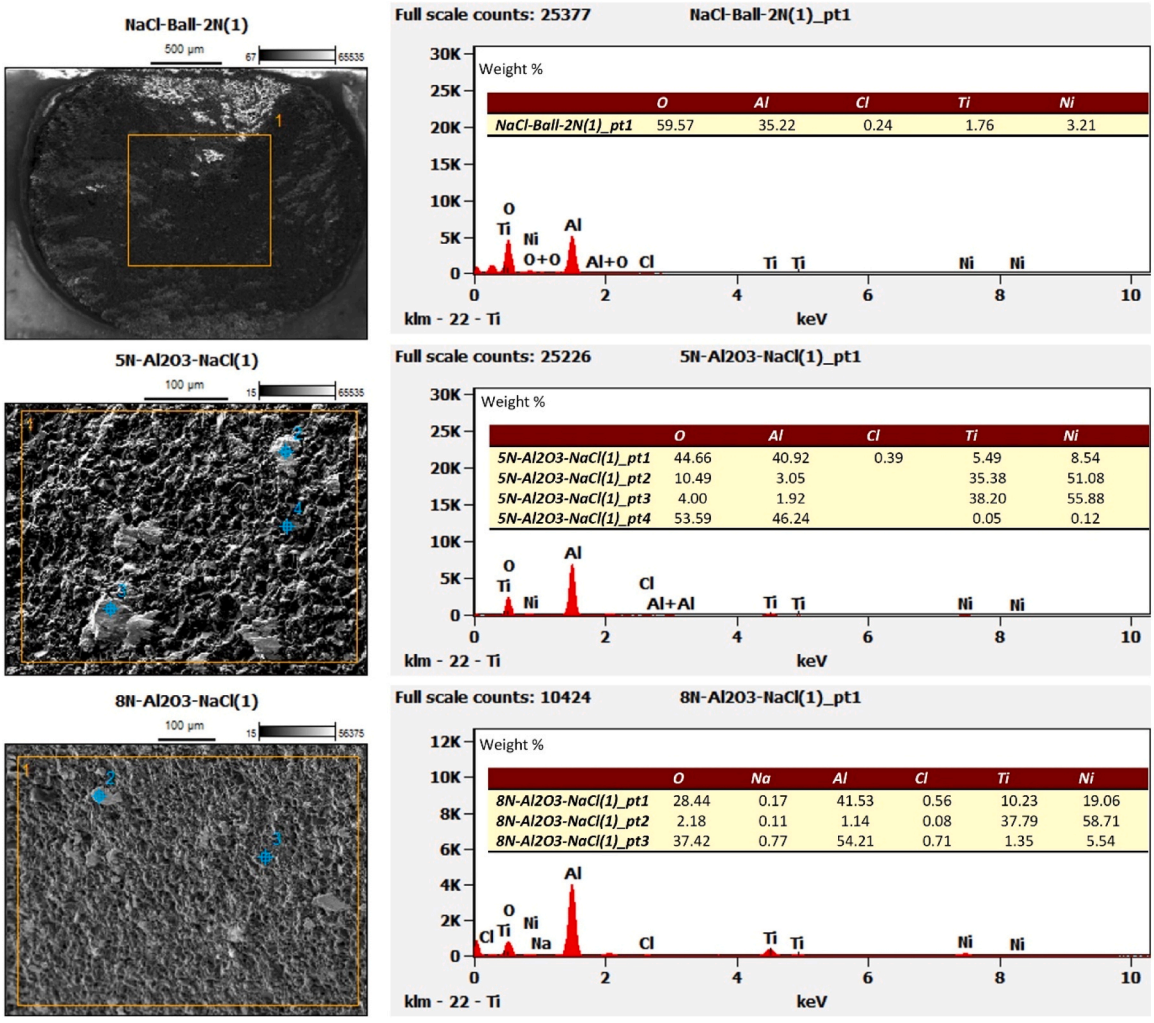

Fig. 8. EDS of Al_2O_3 surfaces sliding against NiTiNOL60 at 2 N, 5 N and 8 N applied loads.

Table 2
Electrochemical parameters estimated from Tafel analysis.

Sample	E_{corr} (V)	$I_{corr} \times 10^{-3}$ (A)	R_p (Ω)	Corrosion Rate (mm/y)
NiTiNOL60 @ 2 N	-2.105	4.784	744.70	1.346
NiTiNOL60 @ 5 N	-1.594	5.473	357.40	2.194
NiTiNOL60 @ 8 N	-1.356	6.588	146.90	2.851

from the applied load evidently contributes to the gradual material detachments and grain refinements or elongations. The SEM results and the evolution of the coefficient of friction with sliding time shown in Fig. 7 confirm that increased applied load increases the contact pressure and the effects of third-body wear, which advances fatigue and crack propagation as sliding contact continues [63]. As a result of the constant sliding of the contact surfaces during linear reciprocating wear tests, the material deforms plastically, which promotes the transfer of wear debris to the opposing body and lowers the rate of corrosive wear [64]. According to the CoF levels, the wear processes caused by the high material detachment occurred due to a synergistic interplay [65] between mechanical and electrochemical actions [25,26,66]. The different stages of pitting and crack propagation, as reported in Section 3.1, highlight the susceptibility of the exposed surface of NiTiNOL60 in NaCl solution. This reveals the need for enhanced hydrophilicity of NiTiNOL60 alloy surfaces in its applications, since the nature of the solution significantly affects the electrochemical response. Additionally, the corrosion potential and current densities promoted the total surface deterioration attributed to the plastic deformation and the active dissolution in the anodic regime. In the cathodic domain, the influence of electrode potential and normal load via tribocorrosion synergy revealed that the samples exhibited similar characteristics as the applied load increased [67].

3.5. Hardness measurements of NiTiNOL60 exposed to NaCl environment for tribocorrosion

A heterogenous distribution of roughness was observed along the wear tracks especially for higher applied loads as a result of the third body wear. Du, et al. [45] reported that the microhardness of NiTiNOL60 fluctuates more violently because of uneven network structures. To validate this information, we evaluated the hardness of the wearing body (NiTiNOL60) before and after the tribocorrosion tests. Using the method described in Section 2, we calculated the hardness by measuring the force applied and comparing it to the geometrical aspects of the indentation, such as the surface area or depth of the indented shapes, diamond (Vicker's) and cone (Rockwell). Accordingly, we measured the Rockwell hardness of a polished sample before the tests and obtained an average value of 62.5 HRC, aligning with the value reported in the literature [16,19,68]. Fig. 12 shows the average results obtained from the micro indentation hardness tests along the sample's

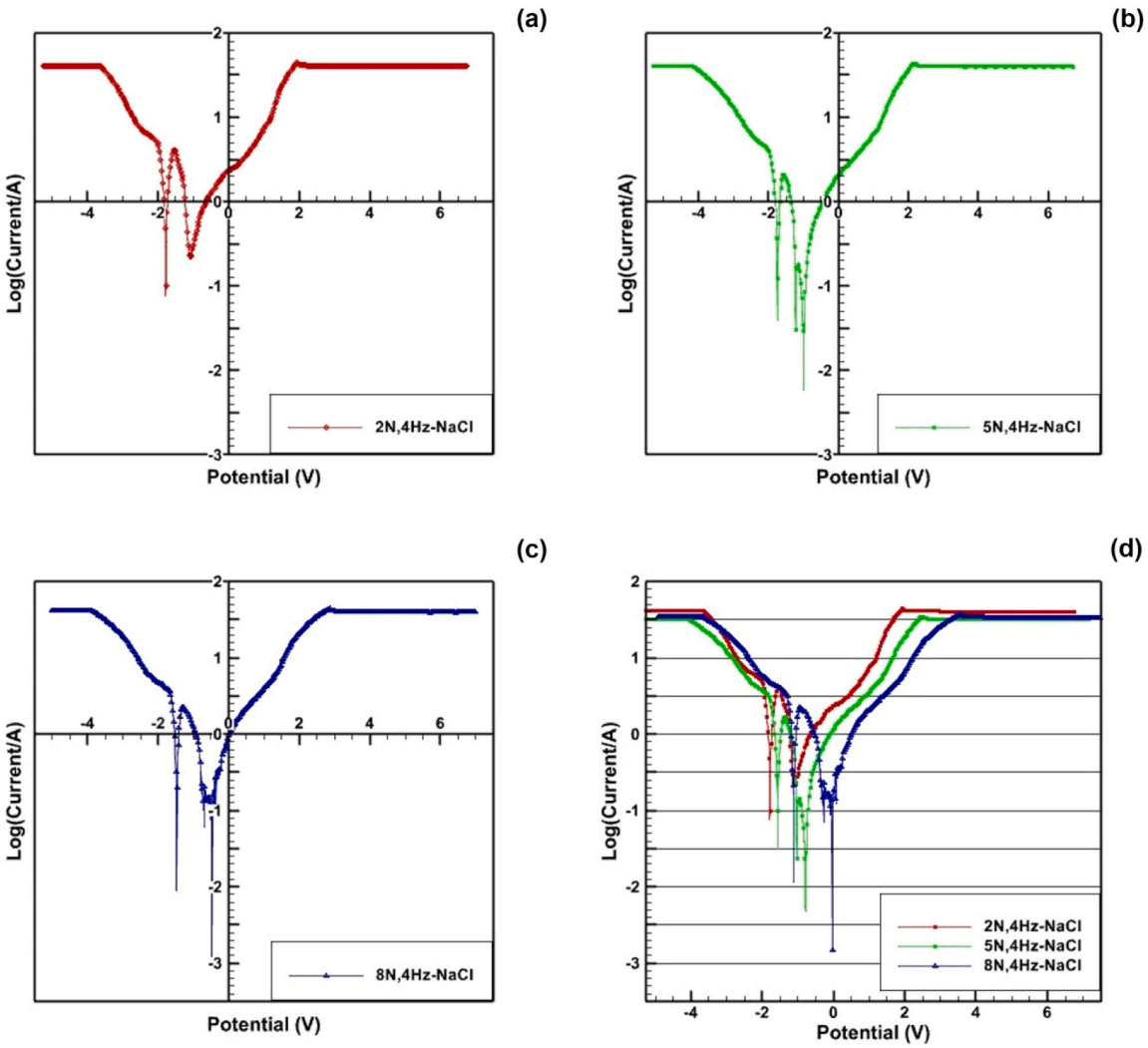

Fig. 9. Tafel plots showing the log current and corrosion potential relationships at different applied loads during tribocorrosion.

wear tracks after each trial. We deduced from the results that the hardness values we measured outside the wear track (i.e., at zero load) show the lowest Vicker's hardness average value of HV 538.44/1.0 kgf/10 s. In contrast, the average Rockwell Hardness value measured for the sample after testing gave an average macro hardness value of 67 HRC. This implies that Rockwell hardness recorded less than a 10% increase during tribocorrosion actions. This could be attributed to different factors, including compressive forces during sliding, friction-induced hardening, and work-hardening of Ni-Ti agglomeration, as well as the repassivation of oxide films, particularly at higher contact pressures [69,70]. The work-hardening due to the reciprocating sliding results in an inhomogeneous distribution of hardness and wear imbalance between the different hardness zones, ultimately causing a deterioration in tribological performance [71]. Supported by the metallographic results, the EDS confirms the formation of oxide layers in the electrolyte medium, while the micrograph in Fig. 3 presented fine eutectic network structures of consolidated and unconsolidated grain clusters. The non-uniformity of the microstructural grains is believed to have been attributed to the low hardness measured outside the wear track, unlike in uniform and fine eutectic network structures where hardness is expected to be higher due to the compact grains.

4. Conclusions

This study delving into the details of wear, corrosion, and their synergistic interactions has shed light on the multifaceted interplay between wear rates, coefficient of friction, applied potential, electrochemical reactions, and the wear-corrosion mechanisms governing the behaviour of NiTiNOL60 alloy. The findings presented in this research offer valuable insights into the complex processes that govern the material's surface and wear track. Our investigation underscores the critical role of equilibrium between passivation and repassivation rates in determining corrosion and wear rate mechanisms. We have confirmed that the progression of corrosion pits, cavities, and cracks is notably accelerated by the presence of sufficient contact pressure at the sliding interfaces, coupled with an increase in corrosion current density. Additionally, the mechanistic interactions promote frictional heating at the contact body interface and asperity shearing at high strain rates during sliding. The observations highlight the profound impact of mechanical forces and electrochemical reactions on the material's surface integrity. Abrasive wear emerged as the predominant wear mechanism, particularly under higher loads. The continuous reciprocating sliding action subjected the contact surfaces to fatigue damage and plastic deformation, resulting in surface degradation. In summary, this study elucidates the synergy between wear and corrosion, revealing their detrimental effects on the surfaces of 60NiTi alloy which will serve as a guide in material selection consideration and the incorporation of this alloy in engineering design. The insights gained from this research contribute to a deeper understanding of the wear-corrosion dynamics, with potential implications for improving the durability and

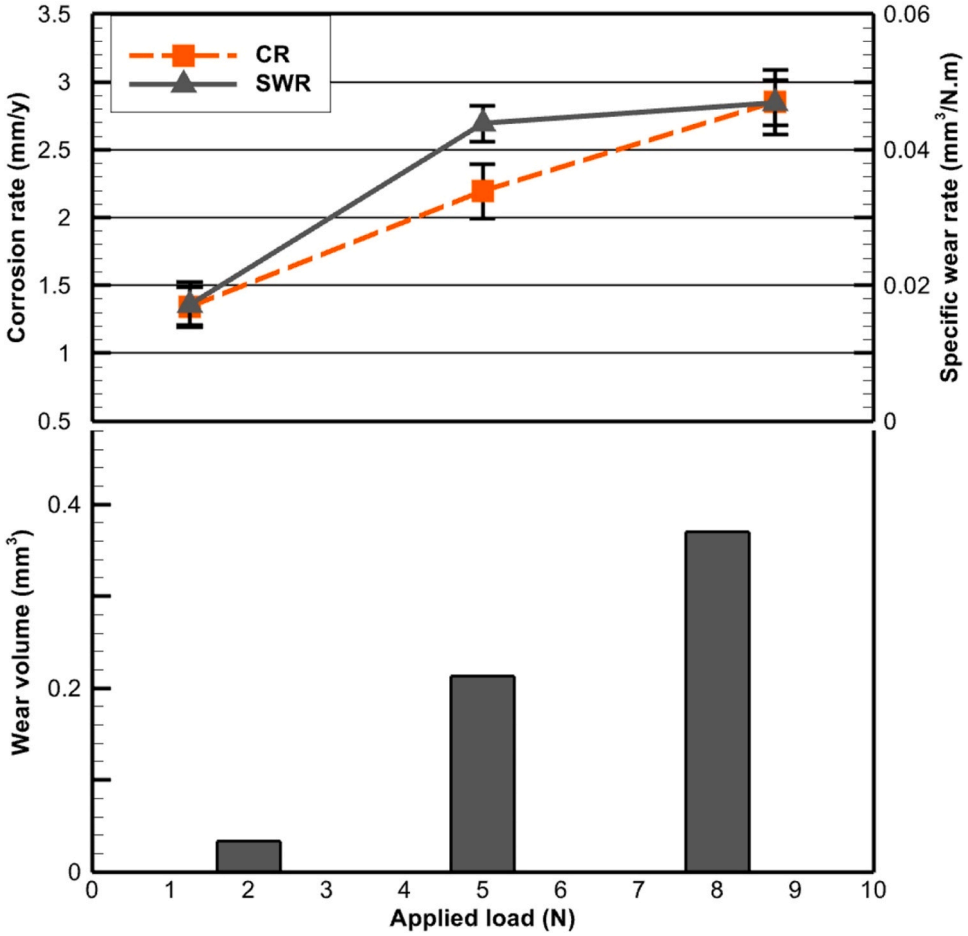

Fig. 10. Wear volume, specific wear rate (SWR) and corrosion rate (CR).

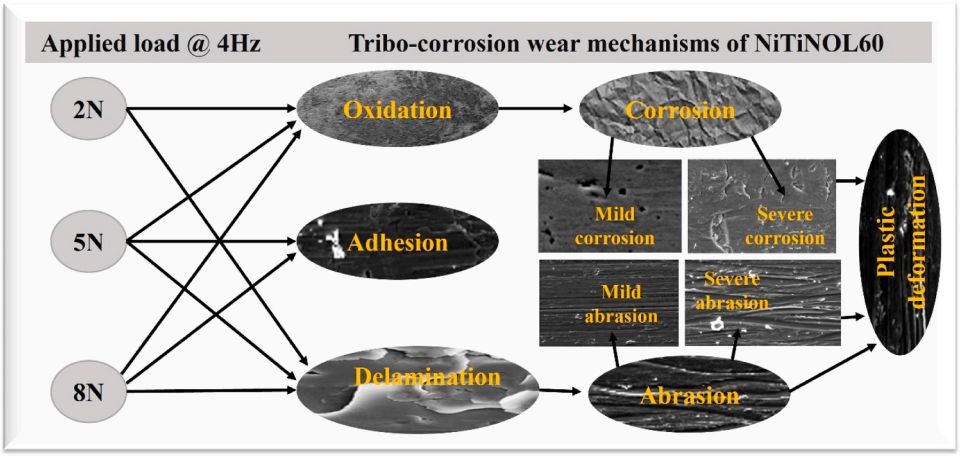

Fig. 11. Simplified representation of tribocorrosion wear mechanisms of NiTiNOL60 alloy.

performance of materials in various engineering and industrial applications. Further research in this direction holds the promise of enhancing the robustness and longevity of critical components subjected to wear and corrosion challenges.

CRediT authorship contribution statement

Anthony Onyebuchi Okoani: Data curation, Formal analysis, Investigation, Methodology, Writing – original draft, Writing – review & editing, Validation, Visualization. **Maziar Ramezani:** Conceptualization, Methodology, Resources, Supervision, Writing – review & editing, Funding acquisition, Validation. **Ashveen Nand:** Methodology, Supervision, Writing – review & editing.

Declaration of Competing Interest

The authors declare that they have no known competing financial interests or personal relationships that could have appeared to influence

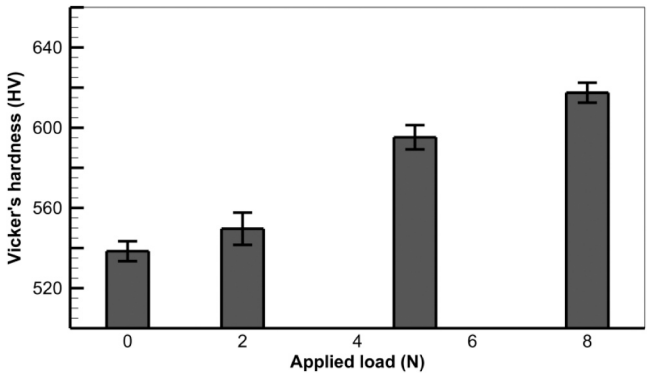

Fig. 12. Graphical representation of the microhardness results.

the work reported in this paper.

Acknowledgment

The authors extend their gratitude to Prof. Christopher DellaCorte for generously supplying the NiTiNOL60 samples used in this study.

References

[1] S. Mischler, A.I. Munoz, Tribocorrosion, in: K. Wandelt (Ed.), in *Encyclopedia of Interfacial Chemistry*, Elsevier, Oxford, 2018, pp. 504–514.
[2] T. Kosec, P. Močnik, A. Legat, The tribocorrosion behaviour of NiTi alloy, Appl. Surf. Sci. vol. 288 (2014) 727–735, https://doi.org/10.1016/j.apsusc.2013.10.116.
[3] R.E. Melchers, Predicting long-term corrosion of metal alloys in physical infrastructure, npj Mater. Degrad. vol. 3 (1) (2019) 1–7, https://doi.org/10.1038/s41529-018-0066-x.
[4] H. Wang, et al., Corrosion behavior of NiTi alloy subjected to femtosecond laser shock peening without protective coating in air environment, Appl. Surf. Sci. vol. 501 (2020) 144338, https://doi.org/10.1016/j.apsusc.2019.144338.
[5] E. Kassab, J. Gomes, Corrosion induced fracture of NiTi wires in simulated oral environments, Art no. 104323, J. Mech. Behav. Biomed. Mater. vol. 116 (2021) 1–6, https://doi.org/10.1016/j.jmbbm.2021.104323.
[6] P. Močnik, T. Kosec, A critical appraisal of the use and properties of nickel-titanium dental alloys, Art no. 7859, Materials vol. 14 (24) (2021) 1–18, https://doi.org/10.3390/ma14247859.
[7] A. López-Ortega, R. Bayón, J.L. Arana, A. Arredondo, A. Igartua, Influence of temperature on the corrosion and tribocorrosion behaviour of high-strength low-alloy steels used in offshore applications, Tribol. Int. vol. 121 (2018) 341–352, https://doi.org/10.1016/j.triboint.2018.01.049.
[8] R. Johnsen, C.B. Von Der Ohe, "16 - Tribocorrosion in marine environments, in: D. Landolt, S. Mischler (Eds.), in *Tribocorrosion of Passive Metals and Coatings*, Woodhead Publishing, 2011, pp. 441–474, ch. 16.
[9] A. López-Ortega, R. Bayón, J.L. Arana, Evaluation of protective coatings for offshore applications. Corrosion and tribocorrosion behavior in synthetic seawater, Surf. Coat. Technol. vol. 349 (2018) 1083–1097, https://doi.org/10.1016/j.surfcoat.2018.06.089.
[10] P. Renner, Y. Chen, Z. Huang, A. Raut, H. Liang, Tribocorrosion influenced pitting of a duplex stainless steel, Lubricants vol. 9 (5) (2021) 1–11, https://doi.org/10.3390/lubricants9050052.
[11] S.V. Pepper, C. DellaCorte, R.D. Noebe, D.R. Hull, and G. Glennon, "Nitinol 60 as a material for spacecraft triboelements," presented at the 13th European Space Mechanisms and Tribology Symposium - ESMATS 13 Conference, Vienna, Austria, September 22-27, 2009, Conference Paper. [Online]. Available: ⟨https://ntrs.nasa.gov/api/citations/20090034488/downloads/20090034488.pdf⟩.
[12] M.J. Carrington, et al., Microstructural characterisation of subsurface deformation and the degradation of Stellite 6 induced by self-mated sliding contact in a simulated PWR environment, Art no. 106899, Tribol. Int. vol. 158 (2021) 1–16, https://doi.org/10.1016/j.triboint.2021.106899.
[13] S. Meddah, et al., Dry sliding wear performance of an annealed TiNi alloy with different nickel contents, Art no. 036508, Mater. Res. Express vol. 7 (3) (2020) 1–10, https://doi.org/10.1088/2053-1591/ab5dea.
[14] M.K. Stanford, "Thermophysical properties of 60-nitinol for mechanical component applications," NASA Technical Report. NASA/TM—2012-216056, Technical Memorandum, GRC-E-DAA-TN-6187 2012. [Online]. Available: ⟨https://ntrs.nasa.gov/citations/20130001731⟩.
[15] C. Dellacorte, S.V. Pepper, R. Noebe, D.R. Hull, Nickel-titanium: A new candidate material for oil-lubricated bearing and mechanical component applications, World Tribol. Congr. 2009 - Proc. (01/01 2009).
[16] C. DellaCorte, "NiTi alloys for tribological applications: The effects of serendipity on research and development.," presented at the Annual Postdoctoral Research and Career Symposium, October 6th. NASA/ GRC-E-DAA-TN34568, Argonne IL., 2016. [Online]. Available: ⟨https://ntrs.nasa.gov/api/citations/20170003993/downloads/20170003993.pdf⟩.
[17] R.C.C. Silva, R.P. Nogueira, I.N. Bastos, Tribocorrosion of UNS S32750 in chloride medium: Effect of the load level, Electrochim. Acta vol. 56 (24) (2011) 8839–8845, https://doi.org/10.1016/j.electacta.2011.07.077.
[18] C. Miller, C. DellaCorte, M. Zou, Nanomechanical properties of hardened 60NiTi, Art no. 14028, Mater. Sci. Eng., A vol. 800 (2021) 1–7, https://doi.org/10.1016/j.msea.2020.140284.
[19] M.K. Stanford, "Hardness and microstructure of binary and ternary nitinol compounds," in "NASA Technical Report," National Aeronautics and Space Administration, Glenn Research Center, No. GRC-E-DAA-TN73728, 2016, issue NASA/TM-2016-218946. [Online]. Available: ⟨https://ntrs.nasa.gov/citations/20160001689⟩.
[20] K. Khanlari, M. Ramezani, P. Kelly, P. Cao, T. Neitzert, An investigation on reasons causing inferiority in unlubricated sliding wear performance of 60NiTi as compared to 440c steel, Tribology Trans. vol. 62 (1) (2019) 96–109, https://doi.org/10.1080/10402004.2018.1516326.
[21] C. DellaCorte, Nickel-titanium alloys for oil-lubricated bearing and mechanical component applications," *Proceedings of*. the ASME/STLE 2009 International Joint Tribology Conference, ASME. Memphis, TN, 2009, pp. 225–227, https://doi.org/10.1115/ijtc2009-15055.
[22] K.J. Yuan, Y. Wang, L.J. Zheng, H. Zhang, Microstructural evolution, mechanical properties, and oxidation performance of highly Ni-rich NiTi alloys with added V using vacuum arc melting, Art no. 160263, J. Alloy. Compd. vol. 877 (2021) 1–10, https://doi.org/10.1016/j.jallcom.2021.160263.
[23] W. Xu, et al., Synergistic interactions between wear and corrosion of Ti-16Mo orthopedic alloy, J. Mater. Res. Technol. vol. 9 (5) (2020) 9996–10003, https://doi.org/10.1016/j.jmrt.2020.06.095.
[24] A. Okoani, A. Nand, M. Ramezani, Tribocorrosion behaviour of NiTiNOL60 alloy in an alkaline environment, Art no. 101305, Results Eng. vol. 19 (2023) 1–11, https://doi.org/10.1016/j.rineng.2023.101305.
[25] A.I. Muñoz, N. Espallargas, "5 - Tribocorrosion mechanisms in sliding contacts, in: D. Landolt, S. Mischler (Eds.), in *Tribocorrosion of passive metals and coatings*, Woodhead Publishing, 2011, pp. 118–152.
[26] C. Yan, Q. Zeng, Y. Xu, W. He, Microstructure, phase and tribocorrosion behavior of 60NiTi alloy, Art no. 143838, Appl. Surf. Sci. vol. 498 (2019) 1–10, https://doi.org/10.1016/j.apsusc.2019.143838.
[27] J. Chen, F.-y Yan, Tribocorrosion behaviors of Ti–6Al–4V and Monel K500 alloys sliding against 316 stainless steel in artificial seawater, Trans. Nonferrous Met. Soc. China vol. 22 (6) (2012) 1356–1365, https://doi.org/10.1016/s1003-6326(11)61326-5.
[28] A. Ayyagari, B. Gwalani, R. Banerjee, T.W. Scharf, S. Mukherjee, C. Barthelemy, Reciprocating sliding wear behavior of high entropy alloys in dry and marine environments, Mater. Chem. Phys. vol. 210 (2018) 162–169, https://doi.org/10.1016/j.matchemphys.2017.07.031.
[29] S. Alkan, M.S. Gök, Effect of sliding wear and electrochemical potential on tribocorrosion behaviour of AISI 316 stainless steel in seawater, Eng. Sci. Technol., Int. J. vol. 24 (2) (2021) 524–532, https://doi.org/10.1016/j.jestch.2020.07.004.
[30] Z. Gao, G. Ji, Z. Shi, X. Wang, The tribocorrosion behaviour of YSZ coating deposited on stainless steel substrate in 3.5 wt% NaCl solution, Ceram. Int. vol. 47 (15) (2021) 21051–21060, https://doi.org/10.1016/j.ceramint.2021.04.107.
[31] M.K. Stanford, "Hot isostatic pressing of 60-Nitinol," NASA Technical Report. NASA/TM-2015-218884, 2015. [Online]. Available: ⟨https://www.techbriefs.com/component/content/article/tb/pub/briefs/manufacturing-prototyping/26497⟩.
[32] S. Mischler, Triboelectrochemical techniques and interpretation methods in tribocorrosion: A comparative evaluation, Tribology Int. vol. 41 (7) (2008) 573–583, https://doi.org/10.1016/j.triboint.2007.11.003.
[33] D. Landolt, S. Mischler, M. Stemp, Electrochemical methods in tribocorrosion: A critical appraisal, Electrochim. Acta vol. 46 (24-25) (2001) 3913–3929, https://doi.org/10.1016/S0013-4686(01)00679-X.
[34] A.I. Munoz, N. Espallargas, S. Mischler, Experimental techniques for tribocorrosion, in: A. Igual Munoz, N. Espallargas, S. Mischler (Eds.), Tribocorrosion, Springer Briefs in Applied Sciences and Technology. Springer, Cham, Switzerland, 2020, pp. 53–64, ch. 6.
[35] ASTM G119-09, "Standard guide for determining synergism between wear and corrosion, Am. Soc. Test. Mater. Book Stand., Vol. 03. 02. Dev. Subcomm. G02. 40 (2021) 1–6, https://doi.org/10.1520/G0119-09R22.
[36] ASTM G133-22, Standard test method for linearly reciprocating ball-on-flat sliding wear, Am. Soc. Test. Mater. Book Stand., Vol. 03. 02. Dev. Subcomm. G02. 40 (2022) 1–10, https://doi.org/10.1520/G0133-22.
[37] S.B. Arya, F.J. Joseph, "Electrochemical methods in tribocorrosion, ISBN: 978-0-12-818916-0, in: A. Siddaiah, R. Ramachandran, P.L. Menezes (Eds.), Tribocorrosion: Fundamentals, methods, and materials, Academic Press, 2021, pp. 43–77. ISBN: 978-0-12-818916-0.
[38] ASTM G3-14, Standard practice for conventions applicable to electrochemical measurements in corrosion testing, Am. Soc. Test. Mater. Book Stand., Vol. 03. 02. Dev. Subcomm. G01. 11 (2019) 1–9, https://doi.org/10.1520/G0003-14R19.
[39] A. Siddaiah, A. Kasar, R. Ramachandran, P.L. Menezes, Introduction to tribocorrosion, in: A. Siddaiah, R. Ramachanran, P.L. Menezes (Eds.), in *Tribocorrosion: Fundamentals, methods, and materials*, Academic Press, 2021, pp. 1–16, ch. 1.
[40] G.A. Rodríguez-Bravo, M. Vite-Torres, J.G. Godínez-Salcedo, Corrosion rate and wear mechanisms comparison for AISI 410 stainles steel exposed to pure corrosion and abrasion-corrosion in a simulated marine environment, Tribology Ind. vol. 41 (3) (2019) 394–400, https://doi.org/10.24874/ti.2019.41.03.09.

[41] A.I. Munoz, N. Espallargas, S. Mischler, Tribocorrosion phenomena and concepts, in: A. Igual Munoz, N. Espallargas, S. Mischler (Eds.), Tribocorrosion, Springer Briefs in Applied Sciences and Technology. Springer, Cham, Switzerland, 2020, pp. 35–42, ch. 4.
[42] O. Benafan, A. Garg, R.D. Noebe, H.D. Skorpenske, K. An, N. Schell, Deformation characteristics of the intermetallic alloy 60NiTi, Intermetallics vol. 82 (2017) 40–52, https://doi.org/10.1016/j.intermet.2016.11.003.
[43] K. Khanlari, M. Ramezani, P. Kelly, M. Hayat, P. Cao, T. Neitzert, An investigation on microstructural and mechanical properties of porous 60NiTi parts solutionized by different cost-effective methods, Metallogr., Microstruct. Anal. vol. 7 (3) (2018) 334–346, https://doi.org/10.1007/s13632-018-0443-4.
[44] K. Khanlari, M. Ramezani, P. Kelly, P. Cao, T. Neitzert, Mechanical and microstructural characteristics of as-sintered and solutionized porous 60NiTi, Intermetallics vol. 100 (2018) 32–43, https://doi.org/10.1016/j.intermet.2018.06.001.
[45] Z. Du, Z. Hu, Y. Feng, F. Mo, The effect of powder composition on the microstructure and corrosion resistance of laser cladding 60NiTi alloy coatings on SS 316L, Art no. 1104, Metals vol. 11 (7) (2021) 1–16, https://doi.org/10.3390/met11071104.
[46] E. Ghali, Corrosion resistance of aluminum and magnesium alloys: understanding, performance, and testing (Wiley series in corrosion). Hoboken, New Jersey: John Wiley & Sons Inc., Hoboken, New Jersey. ISBN: 978-0-471-71576-4, 2010.
[47] Y. Yan, A. Neville, Bio-tribocorrosion: Surface interactions in total joint replacement (TJR), in: Y. Yan (Ed.), in *Bio-tribocorrosion in biomaterials and medical implants*, Elsevier, 2013, pp. 309–340.
[48] Z. Yi, et al., Interfacial friction at action: Interactions, regulation, and applications, Friction (2023) 1–28, https://doi.org/10.1007/s40544-022-0702-x.
[49] I. Hutchings, P. Shipway, "5 - Sliding wear, in: I. Hutchings, P. Shipway (Eds.), in *Tribology (Second Edition)*, Butterworth-Heinemann, 2017, pp. 107–164.
[50] C. Miller, M. Zou, Microscale friction and deformation behavior of polydopamine/polytetrafluoroethylene-coated 60NiTi from nanoscratch tests, Art no. 139079, Thin Solid Films vol. 743 (2022) 1–10, https://doi.org/10.1016/j.tsf.2021.139079.
[51] Q. Zeng, G. Dong, Influence of load and sliding speed on super-low friction of NiTiNOL 60 alloy under castor oil lubrication, Tribol. Lett. vol. 52 (1) (2013) 47–55, https://doi.org/10.1007/s11249-013-0191-1.
[52] I.M. Hutchings, Tribology: friction and wear of engineering materials. Boca Raton: Edward Arnold - A division of Hoddr & Stoughton London. CRC Press. ISBN: 0-340-56184-X, 1992.
[53] J. Yang, Y. Song, K. Dong, E.-H. Han, Research progress on the corrosion behavior of titanium alloys, Corros. Rev. vol. 41 (1) (2023) 5–20, https://doi.org/10.1515/correv-2022-0031.
[54] L. Vilhena, G. Oppong, A. Ramalho, Tribocorrosion of different biomaterials under reciprocating sliding conditions in artificial saliva, Lubr. Sci., Artic. vol. 31 (8) (12/01/ 2019) 364–380, https://doi.org/10.1002/ls.1478.
[55] S. Guadalupe, C. Falcand, W. Chitty, S. Mischler, Tribocorrosion in pressurized high-temperature water: A mass flow model based on the third-body approach, Art no. 10, Tribol. Lett. vol. 62 (1) (2016) 1–13, https://doi.org/10.1007/s11249-016-0653-3.
[56] I. Milošev, B. Kapun, The corrosion resistance of Nitinol alloy in simulated physiological solutions Part 2: The effect of surface treatment, /07/01/ 2012, Mater. Sci. Eng.: C. vol. 32 (5) (2012) 1068–1077, https://doi.org/10.1016/j.msec.2011.08.022.
[57] A. Dalmau, C. Richard, A. Igual – Muñoz, Degradation mechanisms in martensitic stainless steels: Wear, corrosion and tribocorrosion appraisal, Tribol. Int. vol. 121 (2018) 167–179, https://doi.org/10.1016/j.triboint.2018.01.036.
[58] V. Pejaković, V. Totolin, M. Rodríguez Ripoll, Tribocorrosion behaviour of Ti6Al4V in artificial seawater at low contact pressures, Tribol. Int. vol. 119 (2018) 55–65, https://doi.org/10.1016/j.triboint.2017.10.025.
[59] M. Venkatesh, R. Salloom, A.V.M. Rao, A.V. Aditya, "Tribocorrosion mechanisms in sliding contacts,", ISBN: 978-0-12-818916-0, in: A. Siddaiah, R. Ramachandran, P. L. Menezes (Eds.), in *Tribocorrosion: Fundamentals, methods, and materials*, Academic Press, 2021, pp. 79–91. ISBN: 978-0-12-818916-0.
[60] S. Mischler, S. Debaud, D. Landolt, Wear-accelerated corrosion of passive metals in tribocorrosion systems, J. Electrochem. Soc. vol. 145 (3) (1998) 750–758, https://doi.org/10.1149/1.1838341.
[61] G. List, G. Sutter, J.J. Arnoux, Analysis of the high speed sliding interaction between titanium alloy and tantalum, Wear vol. 301 (1-2) (2013) 663–670, https://doi.org/10.1016/j.wear.2012.11.070.
[62] J. Du, S. Cao, A. Igual Munoz, S. Mischler, Tribological and tribocorrosion behavior of nickel sliding against oxide ceramics, Wear vol. 426-427 (2019) 1496–1506, https://doi.org/10.1016/j.wear.2019.01.007.
[63] D. Landolt, S. Mischler, M. Stemp, S. Barril, Third body effects and material fluxes in tribocorrosion systems involving a sliding contact, Wear vol. 256 (5) (2004) 517–524, https://doi.org/10.1016/S0043-1648(03)00561-1.
[64] P. Jemmely, S. Mischler, D. Landolt, Electrochemical modeling of passivation phenomena in tribocorrosion, Wear vol. 237 (1) (2000) 63–76, https://doi.org/10.1016/S0043-1648(99)00314-2.
[65] J.P. Celis, P. Ponthiaux, F. Wenger, Tribo-corrosion of materials: Interplay between chemical, electrochemical, and mechanical reactivity of surfaces, Wear vol. 261 (2006) 939–946, https://doi.org/10.1016/j.wear.2006.03.027.
[66] A. Ghanbarzadeh, F.M. Salehi, M. Bryant, A. Neville, A new asperity-scale mechanistic model of tribocorrosive wear: Synergistic effects of mechanical wear and corrosion, J. Tribology vol. 141 (2) (2019) 1–12, https://doi.org/10.1115/1.4041246.
[67] M.S. Guadalupe, S. Mischler, M. Cantoni, W.J. Chitty, C. Falcand, D. Hertz, Mechanical and chemical mechanisms in the tribocorrosion of a Stellite type alloy, Wear vol. 308 (1-2) (2013) 213–221, https://doi.org/10.1016/j.wear.2013.04.007.
[68] K. Khanlari, M. Ramezani, P. Kelly, P. Cao, T. Neitzert, Reciprocating sliding wear behavior of 60NiTi as compared to 440C steel under lubricated and unlubricated conditions, Tribology Trans. vol. 61 (6) (2018) 991–1002, https://doi.org/10.1080/10402004.2018.1460434.
[69] C. Yan, Q. Zeng, Y. Hao, Y. Xu, M. Zhou, Friction-induced hardening behaviors and tribological properties of 60NiTi alloy lubricated by lithium grease containing nano-BN and MoS2, Tribology Trans. vol. 62 (5) (2019) 812–820, https://doi.org/10.1080/10402004.2019.1619889.
[70] C. Yan, Q. Zeng, W. He, J. Zhu, Enhanced surface hardness and tribocorrosion performance of 60NiTi by boron ion implantation and post-annealing, Art no. 106816, Tribology Int. vol. 155 (2021) 1–11, https://doi.org/10.1016/j.triboint.2020.106816.
[71] Y. Tang, et al., Tribology, corrosion, and tribocorrosion performance of aged lightweight steels: Effects of oxide film and carbide, Art no. 111999, Corros. Sci. vol. 231 (2024) 1–16, https://doi.org/10.1016/j.corsci.2024.111999.